



ALBERT-LUDWIG UNIVERSITY FREIBURG  
Institute of Computer Science  
Chair for Pattern Recognition and Image Processing

**Multiview Deblurring for 3-D Images  
from Light Sheet based Fluorescence Microscopy -  
Supporting Online Material**

**Maja Temerinac-Ott, Olaf Ronneberger, Peter Ochs,  
Wolfgang Driever, Thomas Brox and Hans Burkhardt**

*Technical Report 266*

October 2011



*Chair for Pattern Recognition and Image Processing  
University of Freiburg*

**Multiview Deblurring for 3-D Images  
from Light Sheet based Fluorescence Microscopy -  
Supporting Online Material**

**Maja Temerinac-Ott, Olaf Ronneberger, Peter Ochs,  
Wolfgang Driever, Thomas Brox and Hans Burkhardt**

University of Freiburg  
Institute of Computer Science  
Chair for Pattern Recognition and Image Processing  
Georges-Koehler-Allee Geb. 052  
79110 Freiburg, Germany  
Telephone +49 761 203 8275, Fax +49 761 203 8262  
e-mail: [temerina@informatik.uni-freiburg.de](mailto:temerina@informatik.uni-freiburg.de)

*Technical Report 266*

October 2011



## Abstract

This report provides additional results on multiview deblurring and accompanies the work in [11]. In particular, we provide images of all data sets before and after reconstruction. Moreover, we give more insights into the point spread function (PSF) of the Single Plane Illumination Microscope (SPIM) theoretically and empirically. Finally, the influence of the number of views on the resolution in frequency space is discussed.

## 1 Introduction

Single Plane Illumination Microscopy (SPIM) [4] is a powerful tool for recording deep inside live embryos. It combines the advantages of widefield and confocal microscopy to produce images of high resolution of e.g. zebrafish embryos. SPIM is fast since it records the whole image plane at once (like the widefield) however it only collects light from one plane which keeps the scattering small. The quality of the images is slightly worse than images recorded with confocal microscopy. Beside the very low photo-damaging and the high recording speed one major advantage of the SPIM setup is its mounting technique inside a gel cylinder which makes the objects to be recorded easily movable. Thus one is able to rotate the gel cylinder easily and take images from the same object from different views. In this way one can compensate for absorption and scattering by just taking another image from a slightly different angle. The resulting recordings comprise a number of different views of the same object which need to be 1. registered and 2. fused.

Many solutions for the post processing of the SPIM images have already been proposed ([9], [7], [5]) and solutions for higher resolved images have been sought on both hardware and software sides. Only a combination of high quality hardware and specialized algorithms for this hardware will lead to good results.

In this work we would like to provide additional results to the multiview-deblurring algorithm proposed in [11]. Our algorithm is termed Lucy-Richardson Multiview Overlap-Save with Total Variation regularization (LRMOS-TV).

## 2 Typical 72h Zebrafish structures

In Fig. 1 we display confocal recordings for some typical zebrafish structures. These images are used as ground truth and are later on artificially degraded by spatially-variant blur and Poisson noise to create training and test datasets.

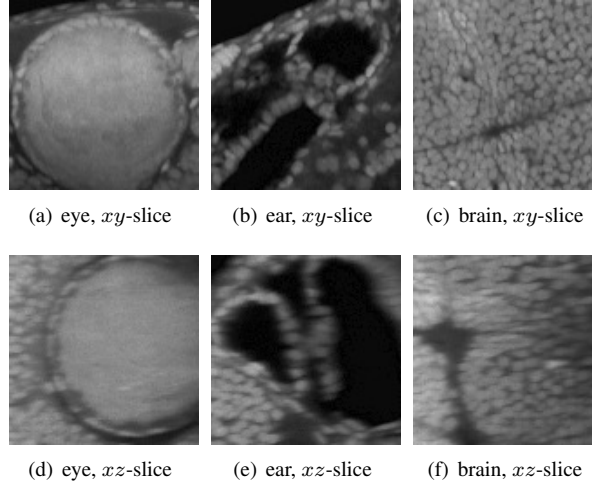


Figure 1: Three 72h zebrafish structures from zebrafish e7 used for the training of the parameter  $\lambda$  representing different textures present in the zebrafish anatomy. The pupil of the eye consists of a large isotropic texture, whereas the brain texture consists of small cells. The top row represents the  $xy$ -slice for  $z = 62$ ; the bottom row is the  $xz$ -slice for  $y = 62$ .

### 3 Multiview Deblurring results for Varying Lambda

We use the Signal-To-Noise-Ratio (SNR) in order to obtain quantitative results. The SNR is defined using the relation between the ground truth image  $u$  and the reconstructed image  $\hat{u}$  as:

$$SNR(u, \hat{u}) = 10 \log_{10} \left( \frac{\sum_{\mathbf{s} \in \Omega_s} (u(\mathbf{s}) - \mu)^2}{\sum_{\mathbf{s} \in \Omega_s} (u(\mathbf{s}) - \hat{u}(\mathbf{s}))^2} \right), \quad (1)$$

where

$$\mu = \frac{1}{|\Omega_s|} \sum_{\mathbf{s} \in \Omega_s} u(\mathbf{s}) \quad (2)$$

is the mean value of the original image.

In Tab. 1 we display the results in terms of the SNR when modifying the regularization parameter  $\lambda$  in the LRMOS-TV algorithm applied to the training data set. It consists of three different structures (ear,eye,brain) from three different data sets (e7,e9,e11). In average the best results are obtained for  $\lambda = 0.002$ . For smooth areas a higher value of  $\lambda$  can be chosen (i.e. eye e7,e9), however this will harm other parts (i.e. brain) which contain more textured structures. Thus, choosing  $\lambda = 0.002$  showed to be the best parameter for deblurring the zebrafish data.

Dataset, structure	$\lambda = 0$	$\lambda = 0.0002$	$\lambda = 0.002$	$\lambda = 0.02$
e7, brain	8.55	8.57	<u>8.72</u>	8.40
e9, brain	10.40	10.44	<u>10.67</u>	10.62
e11, brain	12.40	12.41	<u>12.46</u>	12.06
average, brain	10.45	10.47	<u>10.62</u>	10.36
e7, eye	14.06	13.79	14.15	<u>14.16</u>
e9, eye	13.11	13.16	13.46	<u>13.48</u>
e11, eye	11.28	11.29	<u>11.43</u>	11.21
average, eye	12.94	12.74	<u>13.01</u>	12.95
e7, ear	13.08	13.10	<u>13.23</u>	13.15
e9, ear	13.74	13.78	14.04	<u>14.22</u>
e11, ear	12.84	12.85	<u>12.90</u>	12.76
average, ear	13.22	13.24	<u>13.39</u>	13.38

Table 1: Training of the optimal  $\lambda$ . The SNR after 10 iterations is displayed for different values of  $\lambda$  and three different datasets as well as there average.

Visual results of LRMOS-TV for different values of  $\lambda$  on the eye structure (Tab. 2), the brain structure (Tab.3) and the ear structure (Tab.4) for the training data e7, e9 and e11 are presented. Regularization ( $\lambda = 0.002$ ) suppresses the noise while preserving the image borders.

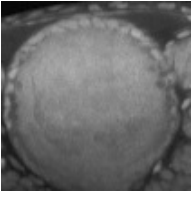
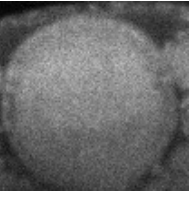
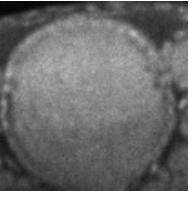
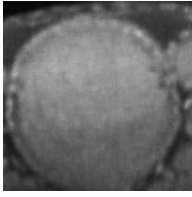
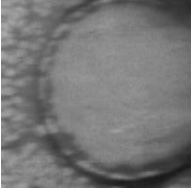
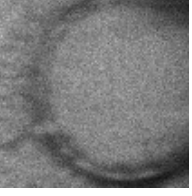
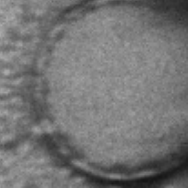
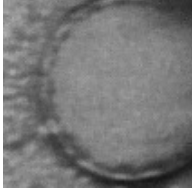
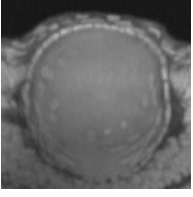
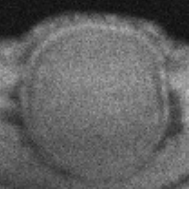
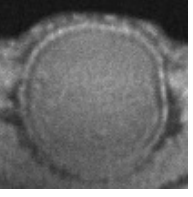
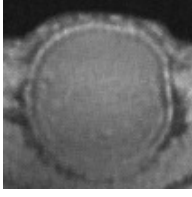
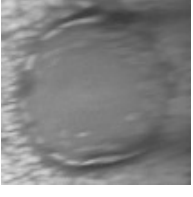
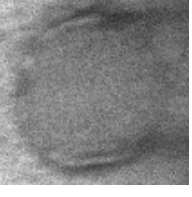
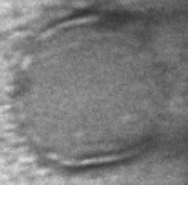
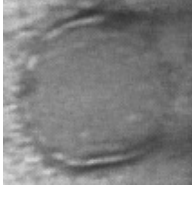
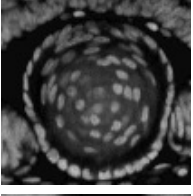
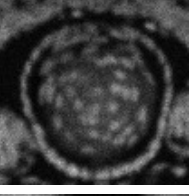
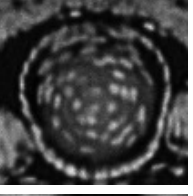
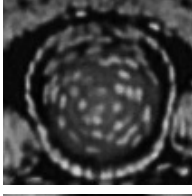
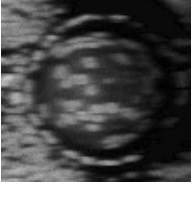

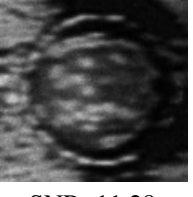
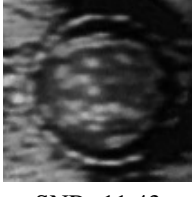
Data set: eye	Original	Degraded	Restored $\lambda = 0$	Restored $\lambda = 0.002$
e7, <i>xy</i> -slice				
e7, <i>xz</i> -slice				
		SNR=11.12	SNR=14.06	SNR=14.15
Data set: eye	Original	Degraded	Restored $\lambda = 0$	Restored $\lambda = 0.002$
e9, <i>xy</i> -slice				
e9, <i>xz</i> -slice				
		SNR=10.84	SNR=13.11	SNR=13.46
Data set: eye	Original	Degraded	Restored $\lambda = 0$	Restored $\lambda = 0.002$
e11, <i>xy</i> -slice				
e11, <i>xz</i> -slice				
		SNR= 9.66	SNR=11.28	SNR=11.43

Table 2: The resulting *xy*-slice and *xz*-slice after performing the LRMOS-TV algorithm for the eye in data sets e7, e9 and e11.

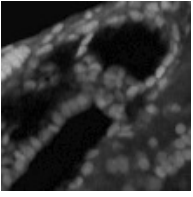
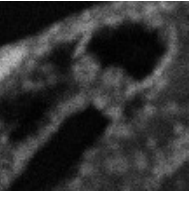
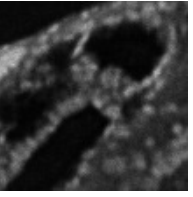
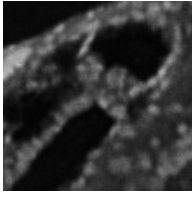
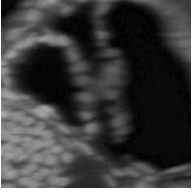
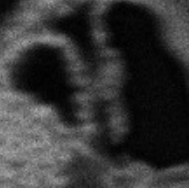
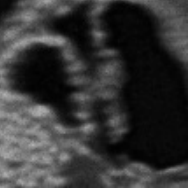
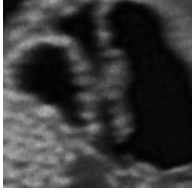
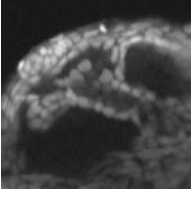
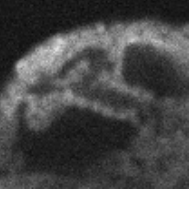
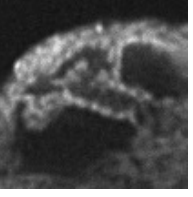
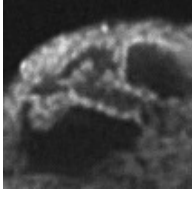

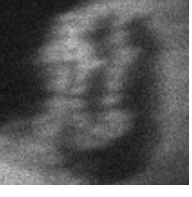


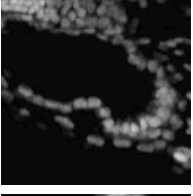
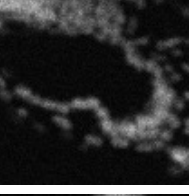
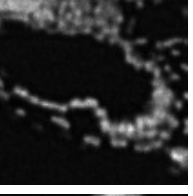
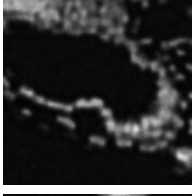

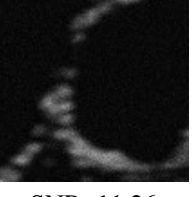


Data set: ear	Original	Degraded	Restored $\lambda = 0$	Restored $\lambda = 0.002$
e7, <i>xy</i> -slice				
e7, <i>xz</i> -slice				
		SNR=10.92	SNR=13.08	SNR=13.23
Data set: ear	Original	Degraded	Restored $\lambda = 0$	Restored $\lambda = 0.002$
e9, <i>xy</i> -slice				
e9, <i>xz</i> -slice				
		SNR=11.27	SNR=13.74	SNR=14.04
Data set: ear	Original	Degraded	Restored $\lambda = 0$	Restored $\lambda = 0.002$
e11, <i>xy</i> -slice				
e11, <i>xz</i> -slice				
		SNR=11.26	SNR=12.84	SNR=12.90

Table 3: The resulting *xy*-slice and *xz*-slice after performing the LRMOS-TV algorithm for the ear in data sets e7, e9 and e11.



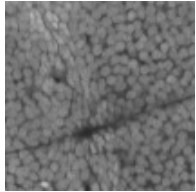
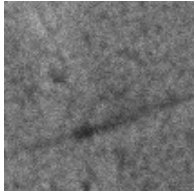
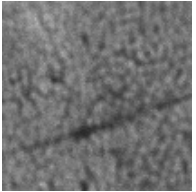
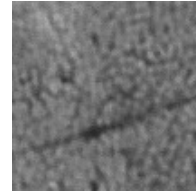
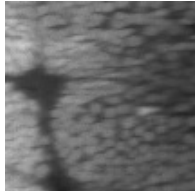
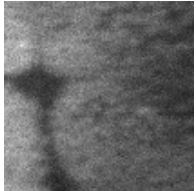
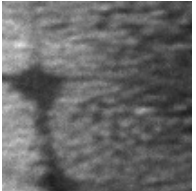
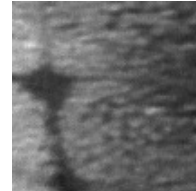
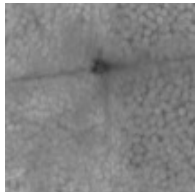
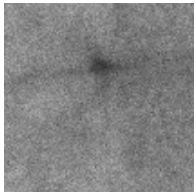
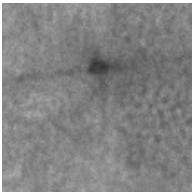
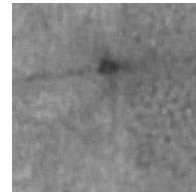
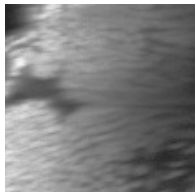
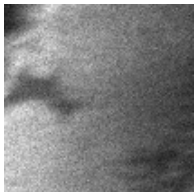
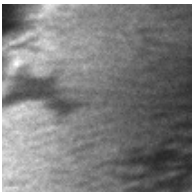

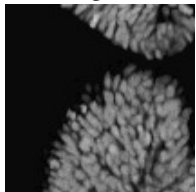
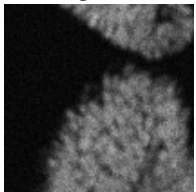
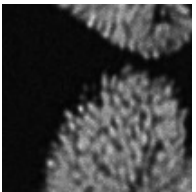
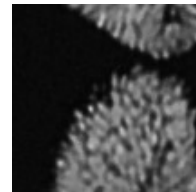
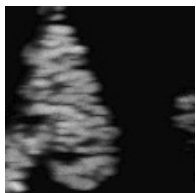
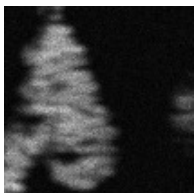
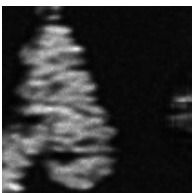
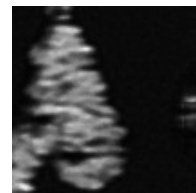
Data set: brain	Original	Degraded	Restored $\lambda = 0$	Restored $\lambda = 0.002$
e7, <i>xy</i> -slice				
e7, <i>xz</i> -slice				
		SNR=6.78	SNR=8.55	SNR=8.72
Data set: brain	Original	Degraded	Restored $\lambda = 0$	Restored $\lambda = 0.002$
e9, <i>xy</i> -slice				
e9, <i>xz</i> -slice				
		SNR=8.85	SNR=10.40	SNR=10.67
Data set: brain	Original	Degraded	Restored $\lambda = 0$	Restored $\lambda = 0.002$
e11, <i>xy</i> -slice				
e11, <i>xz</i> -slice				
		SNR=10.82	SNR=12.40	SNR=12.46

Table 4: The resulting *xy*-slice and *xz*-slice after performing the LRMOS-TV algorithm for the brain in data sets e7, e9 and e11.

## 4 Comparison to State-Of-the-art Methods

The comparison of LRMOS-TV with state-of-the-art methods (Blending [7], No regularization [6], Regularization and constant PSF [2]) is conducted on the test dataset e6. The  $xy$ - and  $xz$ - slices from the original images of those three structures are given in Fig. 2, Fig. 3 and 4. The reconstructed images are given in Tab. 5 for the ear, Tab. 6 for the eye and Tab. 7 for the brain structure. The LRMOS-TV algorithm perform best in terms of SNR.

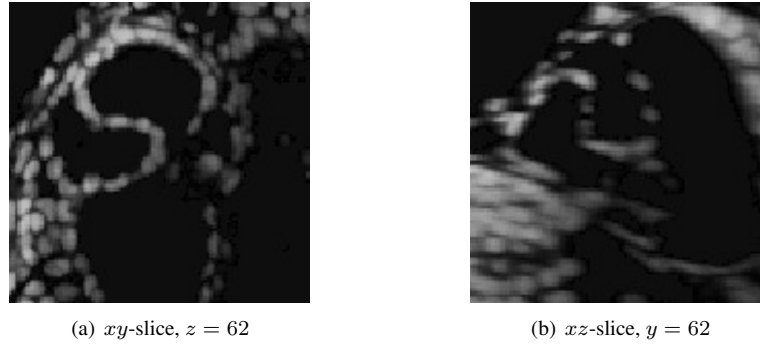


Figure 2: Original image ear e6.

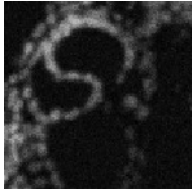
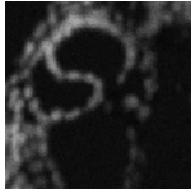
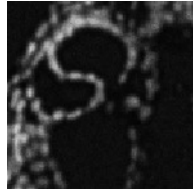
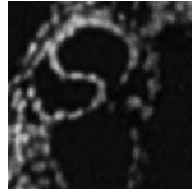
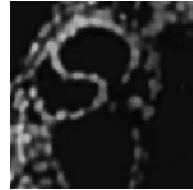
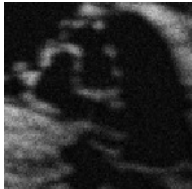
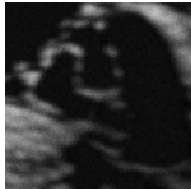

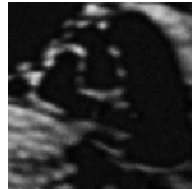

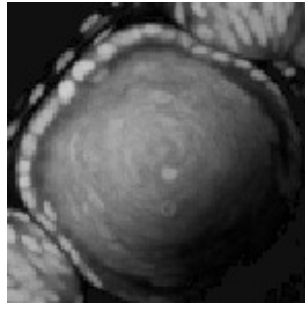
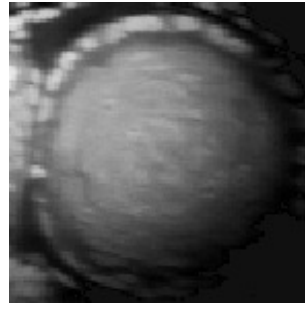
Degraded, view $0^\circ$	Blending [7]	No regularization [6]	Regularization [2]	LRMOS-TV
 $xy$ -slice, $z = 62$				
 $xz$ -slice, $y = 62$ SNR=9.78	 SNR=10.09	 SNR=11.50	 SNR=11.64	 SNR=11.93

Table 5: The resulting  $xy$ -slice and  $xz$ -slice after performing Blending [7], No regularization [6], Regularization [2] and the LRMOS-TV algorithm for the ear in data sets e6.



(a)  $xy$ -slice,  $z = 62$



(b)  $xz$ -slice,  $y = 62$

Figure 3: Original image eye e6.

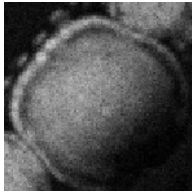
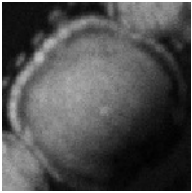
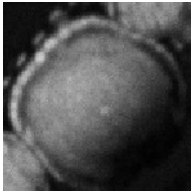
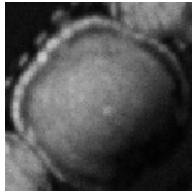
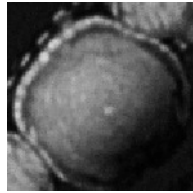
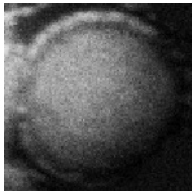
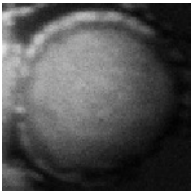
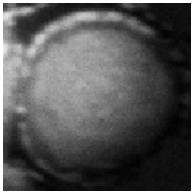
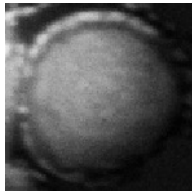
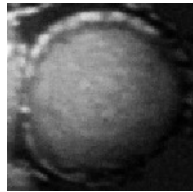
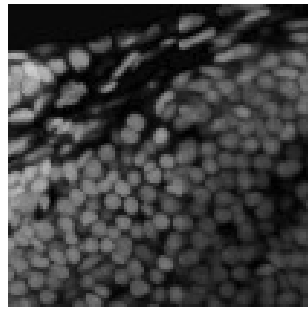
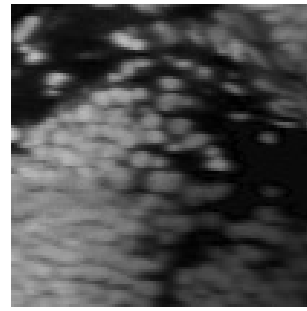
Degraded, view $0^\circ$	Blending [7]	No regularization [6]	Regularization [2]	LRMOS-TV
 $xy$ -slice, $z = 62$				
 $xz$ -slice, $y = 62$ SNR=11.41	 SNR=12.24	 SNR=12.47	 SNR=12.52	 SNR=13.40

Table 6: The resulting  $xy$ -slice and  $xz$ -slice after performing Blending [7], No regularization [6], Regularization [2] and the LRMOS-TV algorithm for the eye in data sets e6.



(a)  $xy$ -slice,  $z = 62$



(b)  $xz$ -slice,  $y = 62$

Figure 4: Original image brain e6.

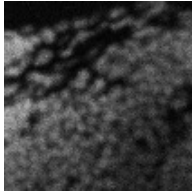
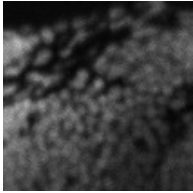
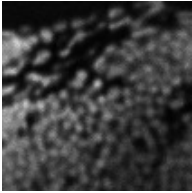
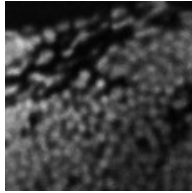
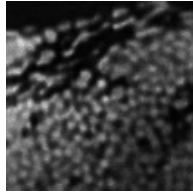
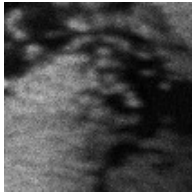
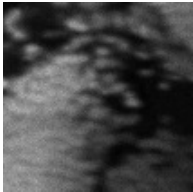
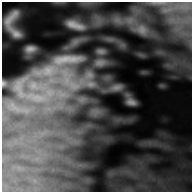
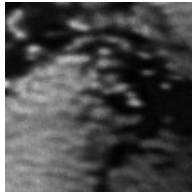
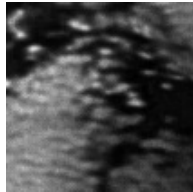
Degraded, view $0^\circ$	Blending [7]	No regularization [6]	Regularization [2]	LRMOS-TV
 $xy$ -slice, $z = 62$				
 $xz$ -slice, $y = 62$ SNR=10.62	 SNR=11.06	 SNR=11.83	 SNR=11.95	 SNR=12.69

Table 7: The resulting  $xy$ -slice and  $xz$ -slice after performing Blending [7], No regularization [6], Regularization [2] and the LRMOS-TV algorithm for the brain in data sets e6.

## 5 Experimental PSF

In Fig. 5 we display the PSFs of six views measured using the same bead. The PSF shape of the SPIM can be approximated by a three-dimensional Gaussian Function [3], however using simply Gaussians to model the PSF is not sufficient to describe the true PSF shape. Due to off-axis lens distortions and small errors during the light sheet alignment, the measured PSF is additionally sheared and no longer perfectly symmetrical.

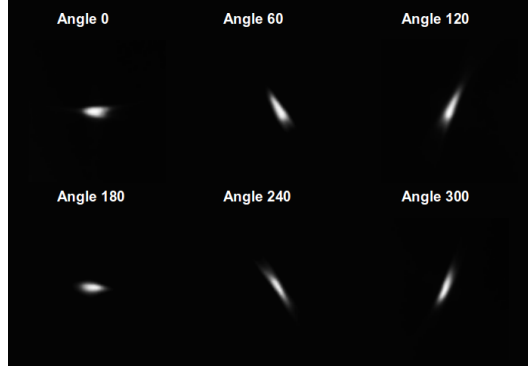


Figure 5: Extracted PSFs from the 6-view acquisition of the zebrafish embryo displayed as  $xz$ -slices.

We have measured the standard deviation of the beads in  $x$ ,  $y$  and  $z$  direction and have found, that the elongation of the bead in axial direction is bigger towards the end of the lightsheet and smaller in the middle of the lightsheet (Fig.6 from [10]). This observation was used to simulate the PSF of the SPIM for generating training and test data sets. The synthetic PSF is computed by a parametric model:

$$H(\mathbf{x}, \mathbf{x}') = \exp\left(-\frac{(x-x')^2 + (y-y')^2}{\sigma^2} + \frac{(z-z')^2}{(4 \cdot x^c \cdot \sigma)^2}\right), \quad (3)$$

where  $\mathbf{x} = (x, y, z)$ ,  $\mathbf{x}' = (x', y', z')$ ,  $x^c = (x - x_{\text{half}})/x_{\text{half}} + 1$  and  $x_{\text{half}}$  denotes half of the size of the  $x$ -dimension size of the image.

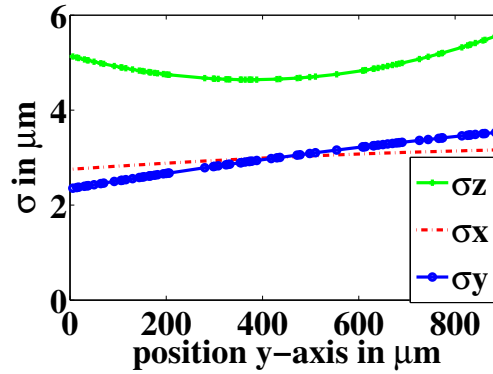


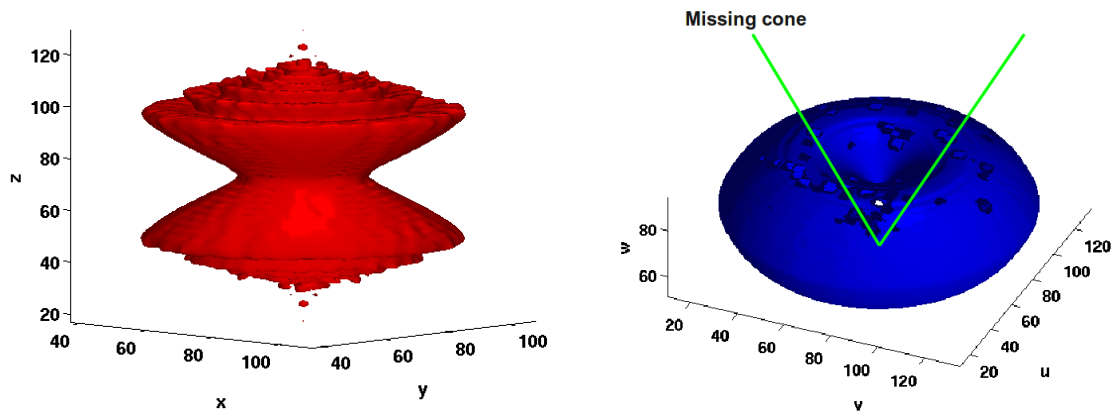
Figure 6: The standard deviation  $\sigma$  along  $x$ ,  $y$ ,  $z$ -axis of a Gaussian fitted to the beads depending on their position in the  $y$ -plane for the original image.

## 6 Missing Cone Problem and Multiview Fusion

The conventional epi-fluorescence widefield microscope suffer from the fact that some frequencies cannot be recorded due to the optical setup of the system. This problem is often referred to as the 'missing cone' problem and can be observed by computing the Fourier transform of the point spread function (PSF) of the system called the optical transfer function (OTF) (Fig. 7 ). Theoretically the OTF can be computed from the numerical aperture (NA) of the used objective and the refractive indices of the immersion medium and the imaged sample [8]. The OTF of the SPIM differs from the traditional widefield PSF (Fig. 8). It is a multiplication of the illumination wide-field PSF and a  $90^\circ$  rotated detection wide-field PSF [3]. Thus the effect of the missing cone is reduced, however the ratio of lateral and the axial extents of the PSF is at best  $1/3$  (e.g. for  $NA = 1.3$ ). Thus the frequency space tends to be well filled along the lateral axes but less well filled along the z-axis.

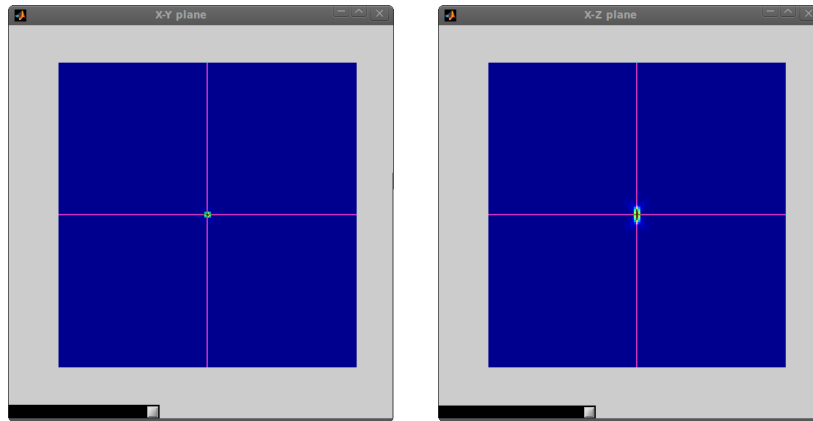
By fusing 3D images from multiple directions the frequency space is filled more evenly. Ideally, the multiple views fill the frequency space isotropically. Under such circumstances, the lateral extents of the single view system PSF dominate the image reconstruction process and the multiview reconstruction provides a better and more isotropic resolution. Two opposing views (i.e. rotation around  $180^\circ$ ) will have almost identical blurring function. Two views orthogonal to each other (i.e. rotation around  $90^\circ$ ) contain more information and will produce a more isotropic resolution. Combining the views will produce a higher resolved image, however the reconstructed PSF will reveal the recording directions. Thus in order to obtain a perfect PSF an infinite number of views should be used. As stated in [6] the ideal number of views depends on several practical parameters: the NA of the lens, the durability of the specimen and available recording and processing time. However, a perfect reconstruction can only be obtained for infinitely many views [1].

We visualize the effect of the multiple views on the OTF of the system schematically in Fig. 9. The minimum cutoff-frequency is reduced if multiple views are used.

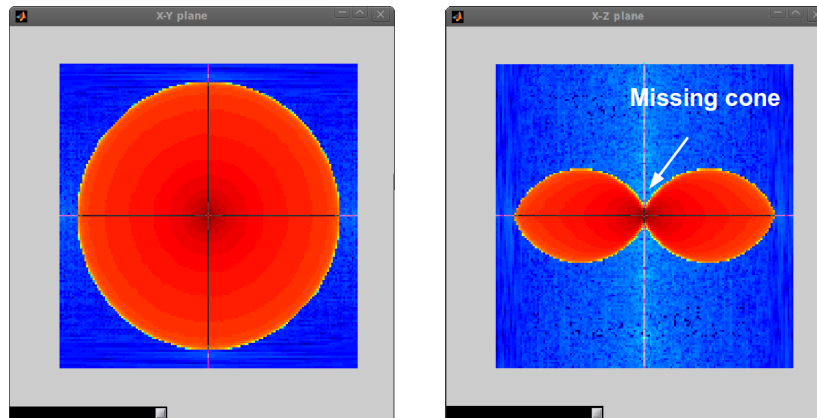


(a) PSF - single view

(b) OTF - single view

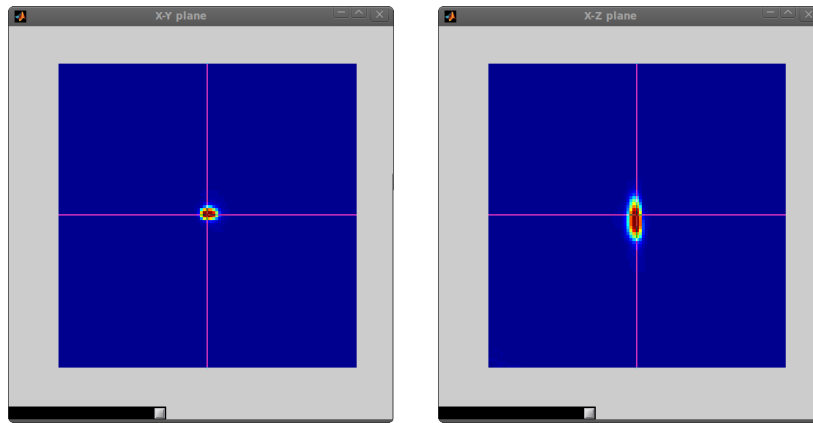


(c) PSF - simulated: central  $xy$ -slice (left) and central  $xz$ -slice (right)

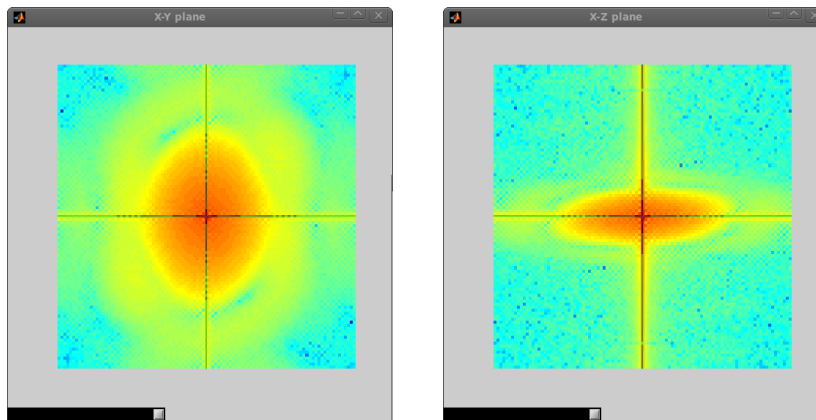


(d) OTF - simulated: central  $xy$ -slice (left) and central  $xz$ -slice (right)

Figure 7: A schematic rendering of the widefield microscopes PSF (a) and OTF (b). Central slices of the same PSF and OTF are displayed in (c) and (d). The coordinates in the spatial domain are referred to as  $x, y, z$  and in the frequency space as  $u, v, w$ . The missing cone is clearly visible in the Fourier domain.



(a) PSF - recorded: central  $xy$ -slice (left) and central  $xz$ -slice (right)



(b) OTF - recorded: central  $xy$ -slice (left) and central  $xz$ -slice (right)

Figure 8: Central slices of PSF and OTF recorded with our SPIM setup are displayed in (a) and (b). The effect of the missing cone is reduced when compared with the simulation of a widefield PSF (Fig. 7).

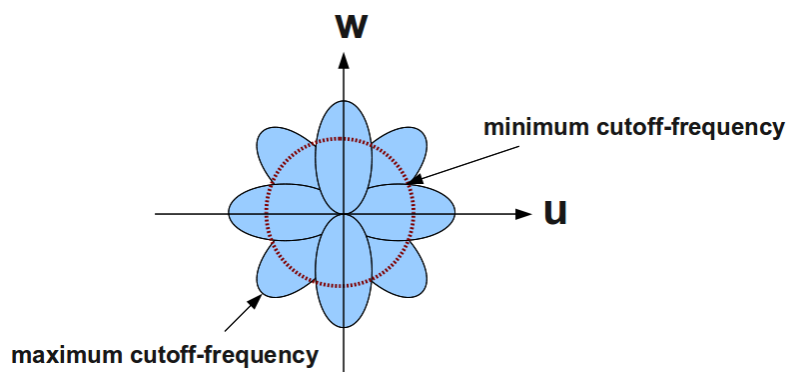


Figure 9: The minimum and the maximum cut-off frequency in the  $uw$ -plane for multiple views. Additional views decrease the minimum cut-off frequency.



## 7 Acknowledgements

This study was supported by the Excellence Initiative of the German Federal Governments (EXC 294) and the SFB 592.

## References

- [1] C. J. Cogswell, K. G. Larkin, and H. U. Klemm. Fluorescence microtomography: Multi-angle image acquisition and 3d digital reconstruction. In *Proc. of SPIE*, volume 2655, pages 109–115, 1996.
- [2] N. Dey, L. Blanc-Feraud, C. Zimmer, P. Roux, Z. Kam, J.-C. Olivo-Marin, and J. Zerubia. 3d microscopy deconvolution using richardson-lucy algorithm with total variation regularization. Technical report, INRIA, 2004.
- [3] J. Huisken. *Multiview microscopy and multibeam manipulation for highresolution optical imaging*. PhD thesis, Universitaet Freiburg, August 2004.
- [4] J. Huisken, J. Swoger, F. D. Bene, J. Wittbrodt, and E. H. K. Stelzer. Optical sectioning deep inside live embryos by selective plane illumination microscopy. *Science*, 305:1007–1009, August 2004.
- [5] P. J. Keller, A. D. Schmidt, A. Santella, K. Khairy, Z. Bao, J. Wittbrodt, and E. H. K. Stelzer. Fast, high-contrast imaging of animal development with scanned light sheetbased structured-illumination microscopy. *Nat. Methods*, 7:637–42, 2010.
- [6] U. Krzic. *Multiple-view microscopy with light-sheet based fluorescence microscope*. PhD thesis, Rupert-Carola University of Heidelberg, 2009.
- [7] S. Preibisch, S. Saalfeld, J. Schindelin, and P. Tomancak. Software for bead-based registration of selective plane illumination microscopy data. *Nat. Methods*, 7:418–419, 2010.
- [8] N. Streibl. Three-dimensional imaging by a microscope. *JOSA A.*, 2:121–127, 1985.
- [9] J. Swoger, P. Verveer, K. Greger, J. Huisken, and E. H. K. Stelzer. Multi-view image fusion improves resolution in three-dimensional microscopy. *Opt. Express*, 15(13):8029–8042, 2007.
- [10] M. Temerinac-Ott, O. Ronneberger, R. Nitschke, W. Driever, and H. Burkhardt. Spatially-variant lucy-richardson deconvolution for multiview fusion of microscopical 3d images. In *Proc. IEEE Int. Symp. Biomed. Imaging*, 2011.
- [11] M. Temerinac-Ott, O. Ronneberger, P. Ochs, T. Brox, and H. Burkhardt. Multiview deblurring for 3-d images from light sheet based fluorescence microscopy. *IEEE Transactions on Image Processing*, 2011. submitted.